Plasma Sources Sci. Technol. **5** (1996) 43–53. Printed in the UK

Discharge equilibrium of a helicon plasma

Isaac D Sudit and Francis F Chen

Electrical Engineering Department, University of California, Los Angeles, Los Angeles, CA 90024-1594, USA

Received 21 March 1995, in final form 27 September 1995

Abstract. The axial dependence of the plasma density, electron temperature, plasma potentials, and the 488 nm argon ion emission intensity have been measured in argon helicon discharges excited by both right helical and Nagoya III antennas for various magnitudes and directions of the magnetic field $\boldsymbol{B}$. The plasma parameters were monitored with RF-compensated probes, while the emission line was detected with an optical emission spectrometer that incorporates an optical fibre and a miniature lens. The right helical antennas were designed to excite the m = +1 azimuthal mode when $\boldsymbol{B}$ is parallel (‖) to the propagation vector $\boldsymbol{k}$, and the m = −1 mode when $\boldsymbol{B}$ is antiparallel (#) to $\boldsymbol{k}$. The plasma is found to be more dense in the former case ($\boldsymbol{B} \parallel \boldsymbol{k}$, m = +1), and the density peaks several antenna lengths downstream in the $\boldsymbol{k}$ direction. Nagoya III antennas are symmetric antennas that should excite the same azimuthal mode content in either magnetic field direction; indeed, the light profile was found to be independent of field direction. In the near field, under the antennas, the density is approximately the same for both antenna geometries and magnetic field directions. These results indicate that the m = +1 mode is preferentially excited regardless of the antenna helicity.

1. Introduction

Helicon sources have been studied extensively and shown to be efficient sources of ionization [1, 2]. They have also been successfully applied to plasma processing [3–6] and have been developed into commercial tools for the manufacture of semiconductor devices [7, 8]. Unlike other inductively coupled plasma (ICP) sources, helicon devices operate by plasma production due to the propagation and absorption of plasma (helicon) waves [9]. This wave propagation and absorption has been studied by several groups [10–13], including ours [14, 15]. The downstream behaviour of the plasma, however, has not been investigated to the same extent as in the case of standard ICP discharges.

In this work we present a comprehensive investigation of the axial variation of argon plasma parameters downstream from an antenna. Plasma density, electron temperature, and plasma and floating potentials have been measured with RF compensated Langmuir probes. The 488 nm Ar^+ plasma emission was monitored with a miniature optical spectrometer. Both of these diagnostics were designed to minimize perturbation of the plasma. In a separate experiment, the propagation of helicon waves has been studied with the aid of magnetic probes [15] and those results are consistent with the ones presented here.

The helicon discharge studied has been described in detail elsewhere [2, 16]. Briefly, the plasma is confined by a 4.7 cm diameter, 165 cm long glass tube, surrounded by solenoid coils that produce the axial magnetic field $\boldsymbol{B} = B\hat{\boldsymbol{z}}$, as shown in figure 1. This field is uniform to ±15% up to the end of the last coil, dropping off rapidly thereafter. The antennas (figure 2) were placed on the outside of the glass tube, closer to the end of the tube that leads to the grounded pumping system. RF current supplied by a 27.12 MHz power supply is fed to the 13–15 cm long antenna through a double-stub tuning network. Argon gas is fed near the midplane of the tube. The discharge conditions for this work are: pulsed discharge with a 50 ms on-time and 1% duty cycle, transmitted power of approximately 2.0 kW with less than 0.2% reflection, Ar pressure of 15 mtorr, and axial magnetic field of 800 G. After about 5 ms, the discharge settles to a steady state which we believe to be the same as would occur in continuous operation, except for the absence of water-cooling and surface changes due to sputtering and deposition.

In helicon discharges, the direction of the axial magnetic field affects the azimuthal mode content and propagation direction of the helicon waves. In this experiment, the effects of this direction was investigated. We have adopted the following nomenclature. We assume that the dominant direction of $\boldsymbol{k}$ is from the antenna to the midplane of the tube. When the magnetic field points in this direction (to the right in figure 1) it will be referred to as a ‘parallel’ (‖) field; when it points towards the pumping port, it will be referred to as an ‘antiparallel’ (#) field.

0963-0252/96/010043+11$19.50 © 1996 IOP Publishing Ltd

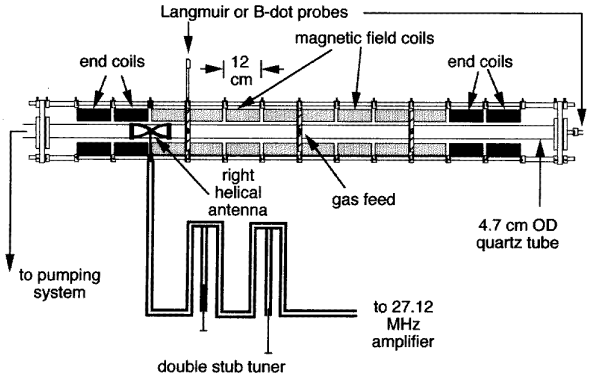

Figure 1. The RF discharge configuration used in this work. The location of the antenna is to scale. The 'standard' conditions will refer to an argon fill pressure of 15 mtorr and 2.0 kW of RF power at 27.12 MHz.

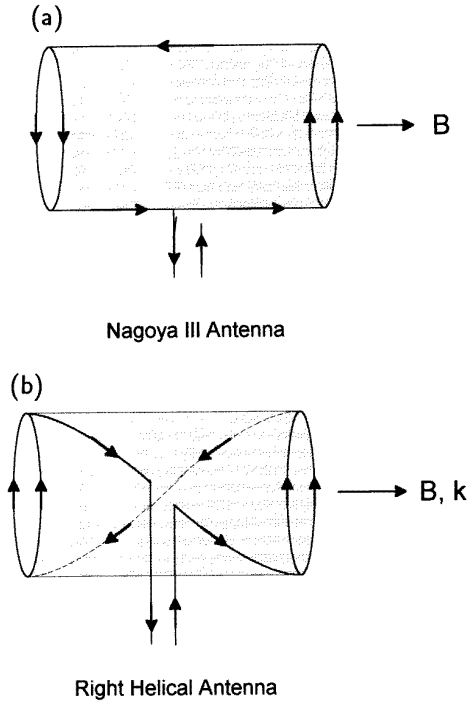

Figure 2. Nagoya III antenna (a) and right helical antenna (b) used to excite helicon waves and to produce the plasma. The arrows show the RF current at one phase. In the case of the right helical antenna, the magnetic field points in the direction of propagation of the $m = +1$ azimuthal helicon mode.

2. Diagnostics

2.1. Langmuir probes

Distortion of the current–voltage curves by oscillating RF plasma potentials has long been recognized as a major obstacle to extracting meaningful results from probe data. To give a properly averaged DC trace it is necessary for the probe tip to follow the potential oscillations at each applied voltage. We have accomplished this by both increasing the circuit impedance of the probe with RF chokes and decreasing the sheath impedance with a floating

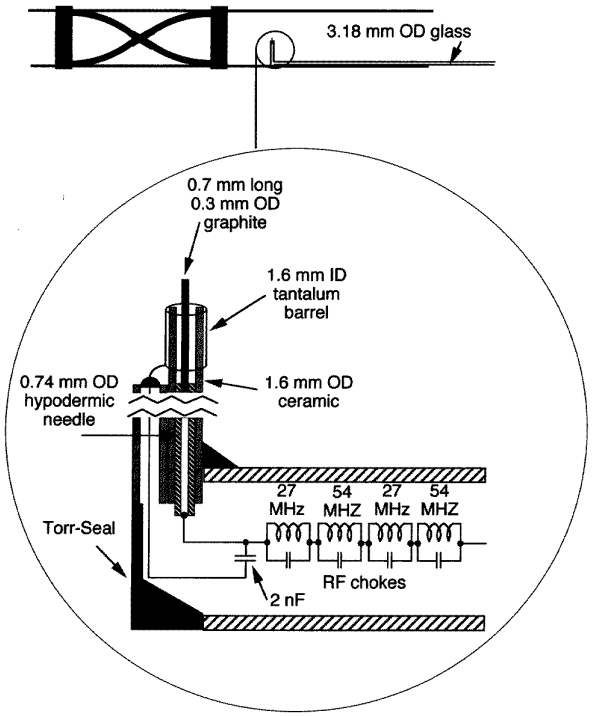

Figure 3. RF compensated Langmuir probe used to measure plasma densities, electron temperatures, and plasma and floating potentials. Individually selected RF chokes provide high circuit impedance at both the first and second harmonics of the RF driving frequency, while the floating tantalum barrel reduces the sheath impedance.

electrode [17] (figure 3). The latter samples the plasma oscillation and forces the probe tip to follow it. It is needed for reducing the distortion of the I–V trace, as shown in figure 4, where beam-like structures appear in the electron retardation region of the curve when only partial RF compensation is used. The 3.18 mm OD, 2 m long glass probe shaft lies on the bottom of the discharge tube, minimizing perturbations to the plasma and allowing for accurate axial and radial positioning of the 0.3 mm OD, 0.7 mm long graphite probe tip. The glass shaft emerges from the discharge through an Ultra-Torr® vacuum fitting, through which it slides to change the probe's axial position. The probe circuit comprises a floating ± 100 V voltage sweeper referenced to ground through a bipolar power supply and a 100 Ω current measuring resistor. Both probe current and voltage were monitored and digitized on an oscilloscope and transferred to a personal computer for analysis. The 2 ms voltage sweep was triggered near the end of the RF pulse to insure that the discharge had reached equilibrium.

The analysis of I–V curves was done as follows. The square of the ion saturation current was fitted to a linear function of probe voltage and subtracted from the total current. The remaining probe current was assumed to be the electron current. The collection of electrons by Langmuir probes is affected by the presence of a DC magnetic field [18, 19]. The I–V curves are particularly distorted near the plasma potential, where cold electrons with small gyroradii are predominant and the saturation

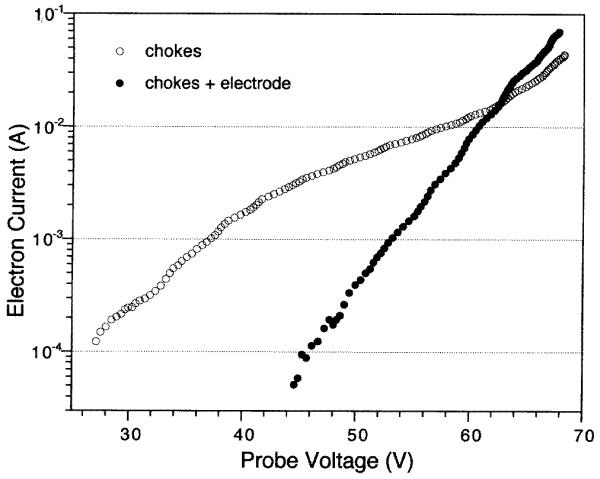

Figure 4. This shows the effect of improper RF compensation on the I–V probe trace. One probe has the full compensation shown in figure 3, while the other has only RF chokes. When full compensation is used, a Maxwellian distribution of electrons is recovered, as illustrated by the two decades of linear dependence between the logarithm of the electron current and the probe voltage. Partial compensation of the plasma oscillations distorts the probe trace and creates spurious beam-like features.

electron current is diffusion limited. We have therefore concentrated on the section of the I–V curve near the floating potential, where magnetic field distortions can be expected to be less severe because only those electrons with large gyroradii outside the sheath can be collected. When the natural logarithm of the electron current is plotted versus the probe voltage, typically two decades of linear dependence are observed, and the slope of the curve is used to deduce the electron temperature T_e. The ion saturation current $I_{ion}(V_f = -100)$, corresponding to a bias voltage 100 V below the floating potential, is used in the following equation, together with the electron temperature, to calculate the plasma density n:

$$I_{ion} = 0.8enA_p(KT_e/M)^{1/2} \tag{1}$$

where A_p is the area of the probe and M is the mass of the argon ion. The constant 0.8 was determined experimentally by calibrating the probe against 62.5 GHz microwave interferometer measurements of the plasma density. For discharges with no axial magnetic fields the plasma potential was unambiguously determined by the maximum of the first derivative of the probe trace. When magnetic fields were present, the first derivative of the probe current is not as peaked as in the zero-field case, and the plasma potential is defined as the voltage at which the first derivative starts decreasing dramatically.

2.2. Optical emission diagnostic

The axial dependence of the 488 nm Ar^+ line was measured with the set-up shown in figure 5. A 3.18 mm OD glass tube is bent at the end to a radius of 1.5 cm and capped with a 2 mm diameter, 2 mm focal length lens using Torr Seal®. The tube rests at the bottom of the glass vessel, with the lens positioned on the axis of the discharge. A 1000 mm long cladded acrylic fibre is inserted in the glass holder and glued in place so its end is approximately at the focal point of the miniature lens. The fibre is coupled into a 0.25 m monochromator through a lens system, and spectral lines are detected with a Hamamatsu R374 photomultiplier tube. The optical probe utilizes the same access port as the one used by the Langmuir probe. This arrangement allows for accurate axial positioning while minimizing plasma disturbance and breaking of the vacuum. The lifetime of the optical detector depends on the heating (and eventual melting) of the plastic fibre and on the erosion of the Torr Seal®. At the duty cycles and RF on-times used, heating of the fibre is not a problem, and the lifetime of the optical system is determined by accidental breaking of the glass holder.

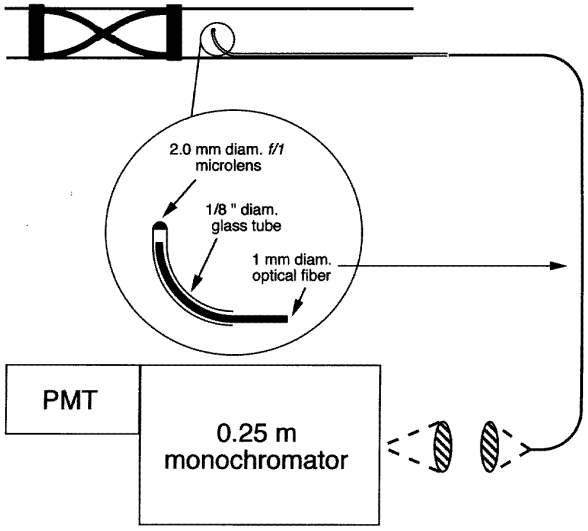

Figure 5. Optical emission spectroscopy system used to measure the axial profile of plasma emission. Measurements were conducted with the miniature lens placed on axis.

3. Results

3.1. Optical emission

3.1.1. Right helical antenna. The axial dependence of the 488 nm Ar^+ line at low magnetic fields for a right helical antenna is shown in figure 6(a) for $\boldsymbol{B} \parallel \boldsymbol{k}$. The shaded areas correspond to the front and back rings of the antenna. For zero field, there is a fairly symmetric emission profile within the antenna region. As the field is increased, however, two distinct peaks appear. The closest to the antenna is under the front ring while the second peak is located about 16 cm from the front ring. In figure 6(b) the profiles for magnetic fields from 0–900 G, at intervals of 100 G, reveal that the second (helicon) peak increases in magnitude but remains fixed in position. The emission profiles are very asymmetric with respect to the centre of the antenna, suggesting preferential plasma production in

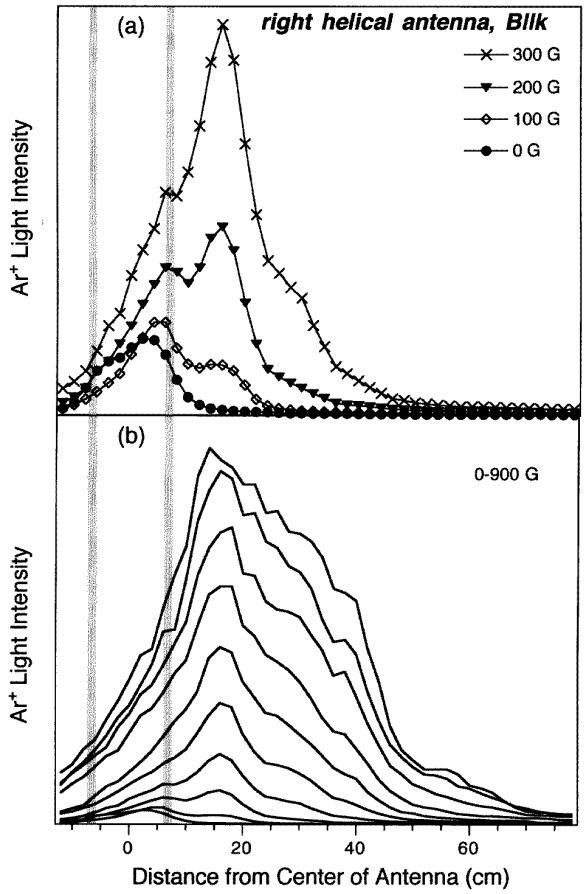

Figure 6. (a) Axial dependence of the 488 nm Ar^+ line intensity for a 'standard' discharge with helical antenna for four magnetic fields. The field is parallel to k (toward the right). The shaded areas correspond to the front and back rings of the antenna. (b) As in (a), but for magnetic fields between 0–900 G at 100 G intervals.

the direction of the magnetic field for this antenna helicity. To investigate this, the axial magnetic field was reversed in direction. A comparison of the emission profiles for two opposite field directions is shown in figure 7. It is evident that the plasma emission peaks away from the antenna, in the direction of the magnetic field.

3.1.2. Nagoya III antenna. The axial dependence of the 488 nm Ar^+ line for a Nagoya III antenna is presented in figure 8. The profiles for zero magnetic field and for the two directions of magnetic field are shown in the same figure. In contrast to the right helical antenna case, the profile is fairly symmetric, with one central peak within the antenna region, and two peaks 16 cm from the centre of the antenna. Notice that the position of these side peaks correspond to the downstream peak for the right helical antenna. Plasma production seems to be insensitive to field direction; the symmetry of the Nagoya III antenna implies equal azimuthal mode content in either direction with respect to the magnetic field. The zero-field profile peaks at the centre of the antenna and is about five times smaller than the helicon profiles.

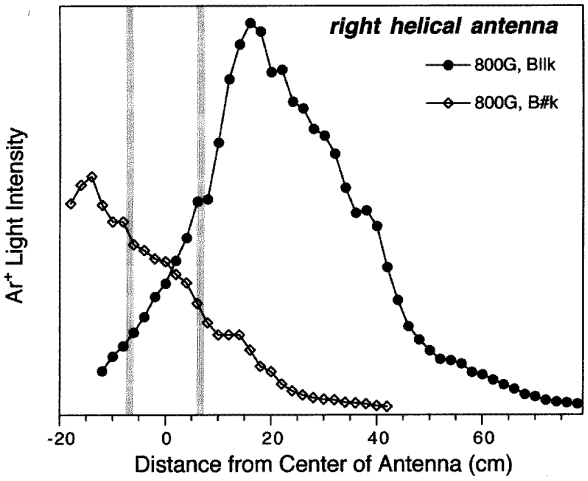

Figure 7. Axial dependence of the 488 nm Ar^+ line intensity for a 'standard' discharge with helical antenna, for B both parallel and antiparallel to k.

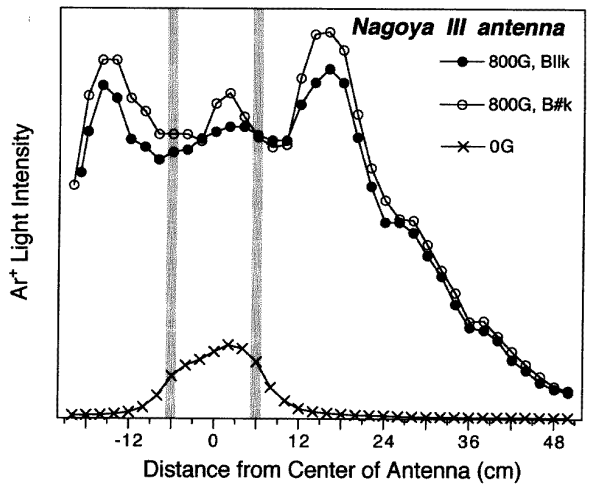

Figure 8. As in figure 7, but for a Nagoya III antenna. The 0 G case is shown for comparison.

3.2. Langmuir probe measurements

Firstly, the standard ICP (no axial field) mode of the helicon discharge was investigated. The electron temperature, plasma density, floating potential V_f, and space potential V_s as a function of distance from the centre of the antenna are shown in figures 9(a) and (b). The density is symmetric about the centre of the antenna, peaking there. This location has also the highest electron temperature. As the plasma diffuses out of the antenna region, it cools down. The rise in T_e at the far end of the tube is believed to be spurious, caused by the failure of RF compensation at the low densities there.

Next, the helicon mode at 800 G was studied. The downstream behaviour of the discharge under these conditions is dramatically different from the ICP mode. The electron density and temperature for a helicon discharge with a right helical antenna and a parallel magnetic field are shown in figure 10(a), and floating and plasma potentials in figure 10(b). Under these conditions, the plasma density

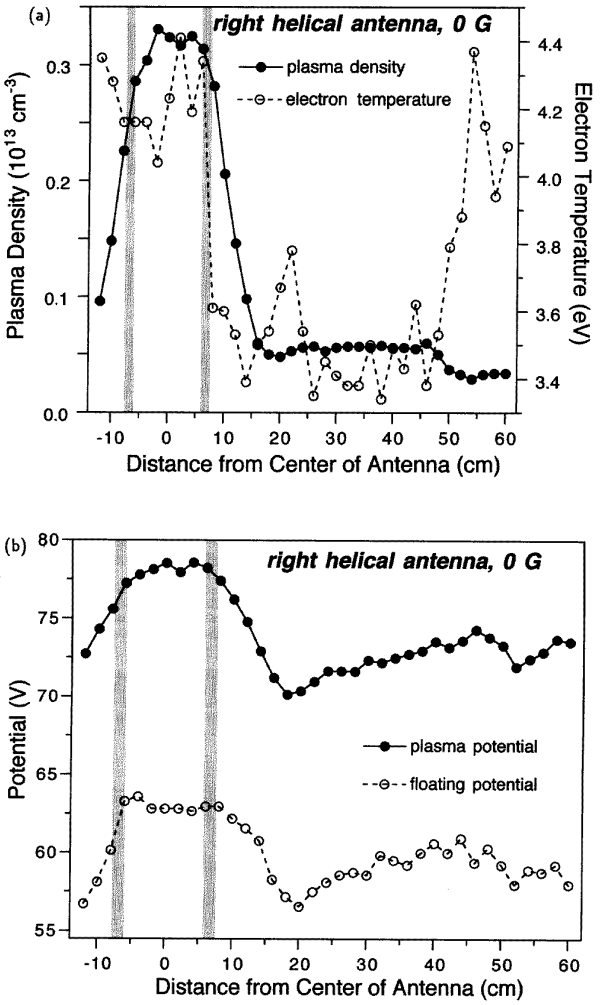

Figure 9. Axial variation of (a) electron temperature and plasma density and (b) plasma and floating potential for a 'standard' discharge with helical antenna in the ICP mode (no axial magnetic field). Zero potential is defined by the ground metal flanges at both ends of the vacuum chamber.

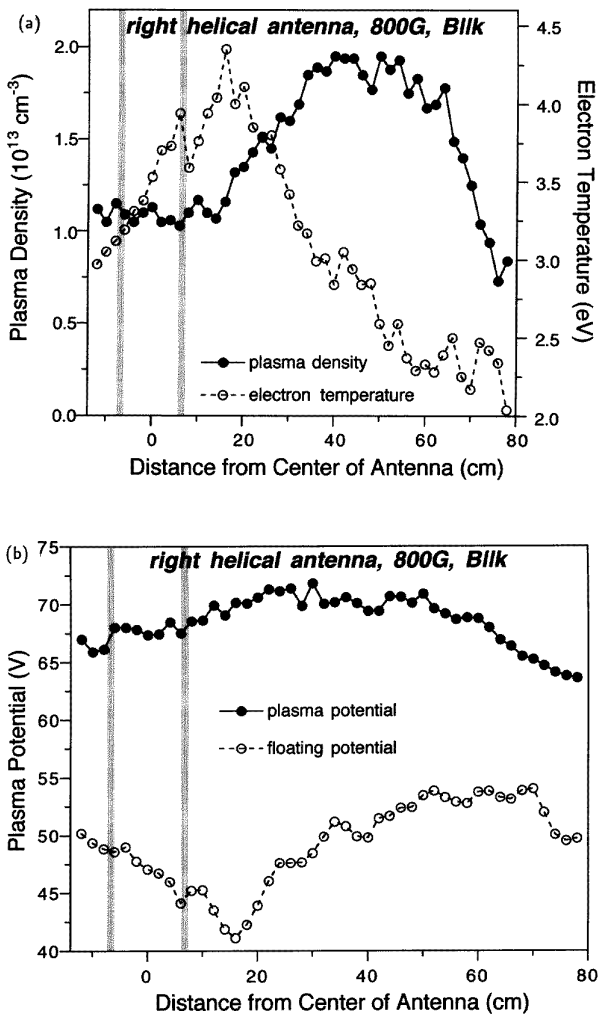

Figure 10. As in figure 9, for an 800 G helicon discharge.

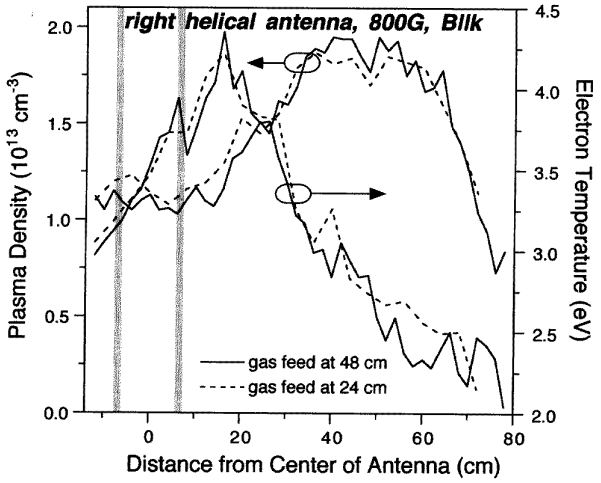

Figure 11. As in figure 10(a), for two different gas-feed locations.

peaks several antenna lengths (50 cm) from the centre of the antenna, while the temperature peaks at approximately 16 cm from the centre. The density within the antenna is fairly uniform and about a factor of two smaller than downstream, while the temperature cools by the same factor downstream. Note that the peak in density is close to the gas feed location (48 cm). To make sure that the downstream density increase is not due to a pressure gradient effect, the gas feed was moved to 24 cm from the centre of the antenna and the measurements repeated. The results shown in figure 11 indicate no change in temperature or density profiles with gas feed location.

As in the case of the optical emission experiments, the dependence of plasma production on the direction of the axial magnetic field and antenna geometry was also studied. The plasma density and electron temperature for the Nagoya III helicon discharge are shown in figure 12. The temperature drops downstream up to about 40 cm, where it starts increasing spuriously, as in the $B = 0$ case, while the plasma density is fairly constant within the antenna region, increasing slightly downstream before finally falling. The plasma densities for the various configurations are compared in figure 13. The peak

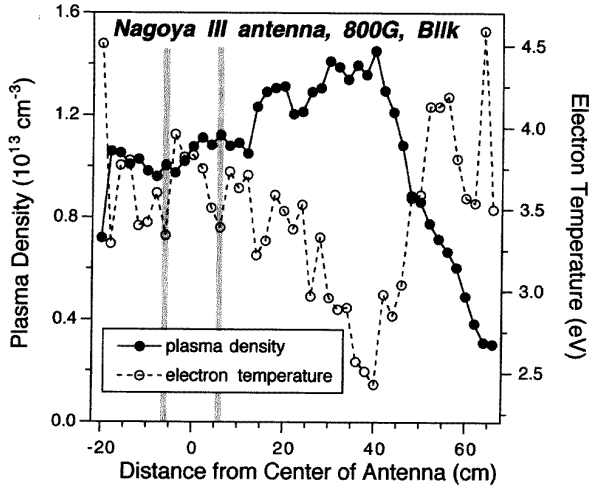

Figure 12. As in figure 10(a), but with a Nagoya III antenna.

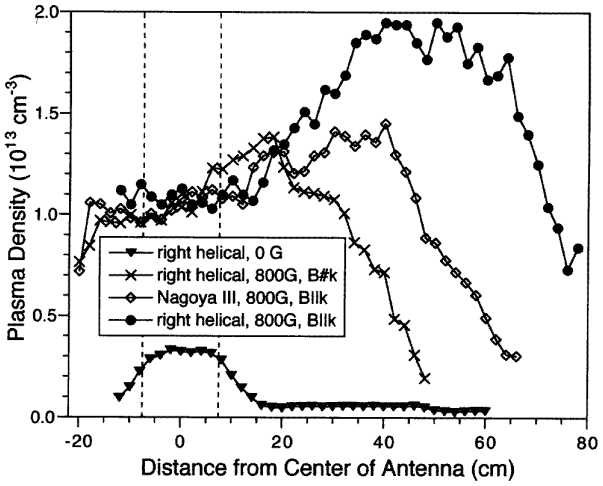

Figure 13. Comparison of axial density profiles for all the discharges studied in this work.

density for standard ICP conditions is about an order of magnitude smaller than for helicon discharges. In the latter, the behaviour of the plasma density depends on the direction of the axial magnetic field. For different antenna geometries and magnetic field directions, the helicon plasma density is basically the same under the antenna but differs downstream. The highest density is achieved with the right helical antenna with parallel field, conditions conducive to the excitation of the $m = +1$ mode. The power allocated to this azimuthal mode can be expected to be lower when a Nagoya III antenna is used since the geometry allows for the excitation of the $m = +1$ mode in the opposite direction as well. This is reflected in the lower peak density and shorter plasma column produced with this antenna. As previously discovered in radial and axial helicon wave investigations [14, 15], we cannot excite the $m = -1$ mode efficiently, as demonstrated by the short plasma length generated with $\boldsymbol{B} \# \boldsymbol{k}$. Presumably this is due to the high density required for the excitation of this mode, unattainable at the RF powers available to us, and to the sharp radial field profile of the $m = -1$ mode, making it difficult to couple to the antenna [15].

4. Analysis

4.1. Evidence for plasma production by waves

Previous investigations of the radial profiles of helicon waves [14] and a more recent study of the axial propagation of these waves [15] have revealed the asymmetry of plasma properties and wave propagation with respect to the direction of the magnetic field for helical antennas. These results, and the ones presented here, confirm that helicon discharges are not ICP plasmas in which waves incidently arise, but plasmas excited by waves. The magnetic field not only plays a confinement role (which would be independent of magnetic field direction) but also allows for the propagation of these whistler waves and the operation of the discharge in the distinct helicon mode.

The optical emission results suggest that at high power levels there is a smooth transition from the ICP to the helicon mode as the axial magnetic field is increased. The emission profiles for both the helical and the Nagoya III antenna evolve from antenna-peaked to downstream-peaked, with a peak underneath the front ring of the antenna at low field values. Why a similar peak beneath the back ring of the helical antenna is not seen under these conditions is not understood but may be due to decreased confinement there, since the field lines flare out to the wall near the end of the uniform-field region. The downstream peaks of the 488 nm Ar^+ line occur at 16 cm from the centre of the antenna for both antenna geometries and remains fixed in location regardless of the magnetic field applied. This peak, however, has been observed to move downstream when the neutral pressure is decreased, suggesting that its position is connected with the electron mean free path.

4.2. Optical emission profile

The electron temperature measured with Langmuir probes peaks at the same location as the optical emission. This is to be expected, since the emission intensity is primarily a function of T_e. We now calculate the emission profile from the measured n and T_e profiles. The 488 nm Ar^+ emission line corresponds to the transition 4p $^2D^0_{5/2} \rightarrow$ 4s $^2P_{3/2}$. If the upper level is assumed to be populated by electron impact excitation of the ground state of the Ar^+ ion, the emission intensity I_{em} is proportional to:

$$I_{em}(z) \propto n^2(z)\overline{\sigma_x v}(z) \qquad (2)$$

where z is the distance along the axis from the centre of the antenna, $\sigma_x(v)$ is the cross section for impact excitation by electrons with speed v, and the average is over the electron velocity distribution, which depends on z through T_e. The cross section for the excitation of the 4p $^2D^0_{5/2}$ level measured by Imre *et al* [20], together with the measured electron densities and temperatures, was used

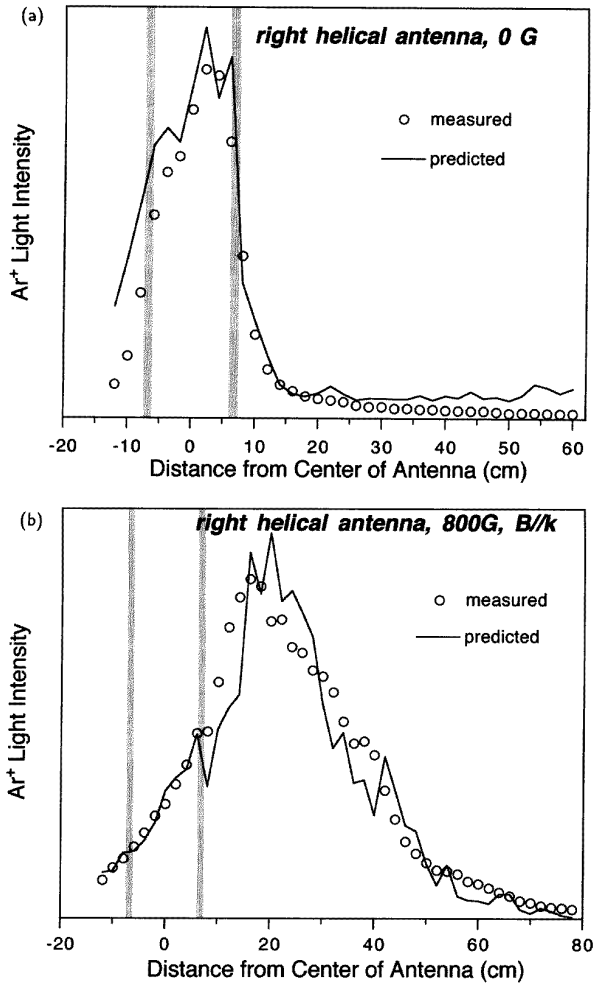

Figure 14. Comparison of calculated (line) and measured (points) Ar^+ line intensities for the 'standard' discharge at (a) 0 G and (b) 800 G.

in equation (3) to predict the optical emission profiles, assuming a Maxwellian distribution of energies. We have also assumed the radial profile of n to be unchanged along z, and of T_e to be flat at all z. Figures 14(a) and (b) show the measured and calculated profiles for a $B = 0$ and $B = 800$ G ($\boldsymbol{B} \parallel \boldsymbol{k}$) helicon discharges, respectively, with the absolute scale adjusted for best fit. Very good agreement is observed in both cases. Similar calculations have been carried out for excitation of the $Ar^+4p\ ^2D^0_{5/2}$ level from the ground states of the neutral atom and the metastable ion, but no agreement between measured and calculated profiles was obtained. As further proof that excitation from the ground state of the ion is dominant, we computed the relative densities for 800 G and 0 G using the measured line intensities and temperatures, assuming that the emission is proportional to n^2, rather than n. The result, shown in figure 15, agrees well with the measured densities.

4.3. Pressure balance

The most puzzling feature appearing in the data is the downstream peak in density, which, for the helical antenna,

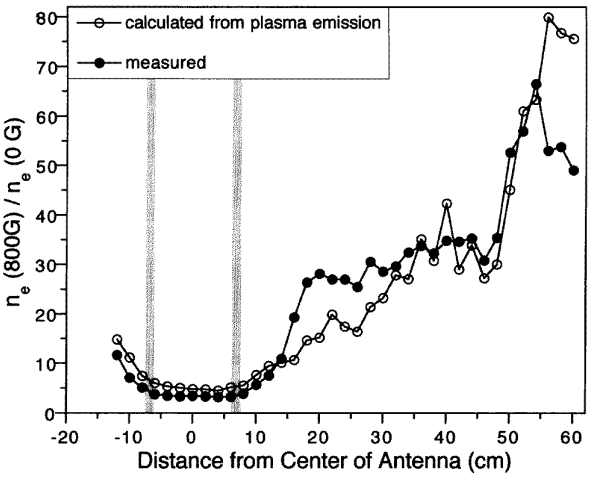

Figure 15. Ratio of plasma density at 800 G to that at 0 G as calculated from the measured line intensity (○) and as directly measured (●).

occurs at $z \approx 50$ cm. As will be seen later, at that position the ionization rate is low and the diffusion rate is large, so that production and loss mechanisms would not be expected to produce a peak. We have been able to explain the peak in terms of pressure balance. In figure 10(a), it is seen that T_e peaks near the antenna and then decays monotonically downstream. This decay length will be calculated later, but if we take $T_e(z)$ and $V_s(z)$ for the moment as given, the density behaviour can be explained quantitatively. Because of their large mobility along field lines, the net parallel force on the electrons must nearly vanish. As T_e decays, n must rise to keep the pressure nKT_e constant. A large electric field cannot arise to balance the pressure gradient because the conductivity is high enough to prevent this. That E_z is indeed small can be seen in the $V_s(z)$ curve shown in figure 10(b).

To be specific, the z component of the electron equation of motion is, in steady state,

$$-enE_z - \partial(nKT_e)/\partial z - mn\nu_m u_z = 0 \qquad (3)$$

where u is the electron fluid velocity and ν_m the electron collision frequency for momentum transfer. Though this collision term is shown for completeness, in practice it is negligibly small. The first two terms of equation (3), representing the electric and pressure-gradient forces per unit volume, can each be calculated for each z from the measured n, T_e, and V_s profiles. These terms are shown for the ICP discharge in figure 16(a). The axial forces on the electron fluid are seen to be equal and opposite, balancing each other along the length of the discharge. This is not surprising, since no significant axial flow of electrons is expected in the bulk of these discharges. Both the electric and pressure-gradient forces have the greatest magnitude under the rings of the antenna. The location of the grounded flange where the gas is fed into the discharge is evidenced by the feature approximately 48 cm from the centre of the antenna.

The corresponding curves for the 800 G helicon discharge are shown in figure 16(b). The electric and

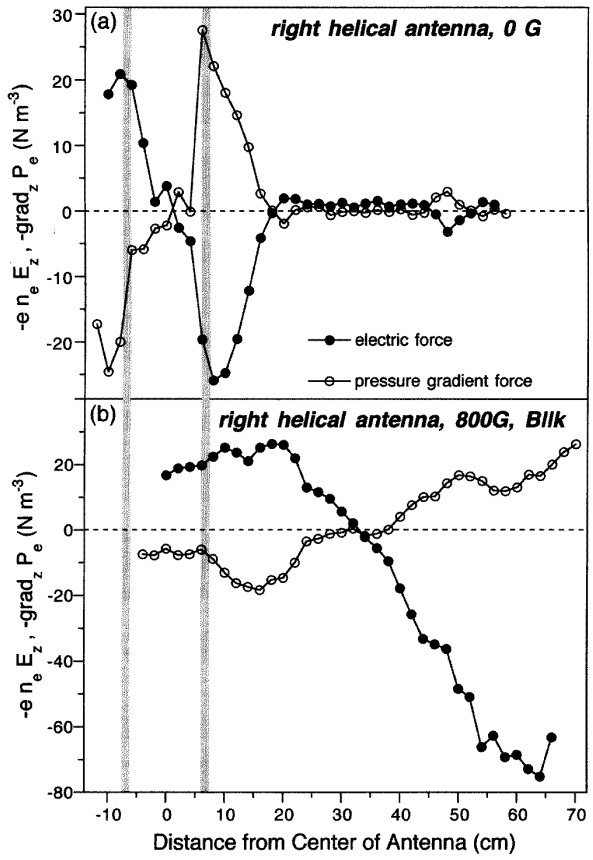

Figure 16. (a) Electric and pressure gradient forces on the electron fluid for a 0 G ICP discharge under 'standard' conditions. (b) Same for an 800 G helicon discharge.

pressure-gradient forces are everywhere opposite, but not exactly equal. We believe that the error lies mainly in the calculation of E_z, since the space potential is difficult to obtain from the probe characteristics in a strong magnetic field. The downstream density peak is therefore required by pressure balance, given the $T_e(z)$ and $V_s(z)$ profiles. The ions are moved slowly by small electric fields to preserve quasineutrality in this equilibrium.

4.4. Particle and energy balance

The steady-state equation of continuity for either species is

$$Q = -\nabla \cdot (D_a \nabla n) \tag{4}$$

where Q is the production rate of ion-electron pairs per unit volume and D_a the ambipolar diffusion coefficient. For an azimuthally symmetric plasma of radius a, $Q(r, z)$ is given by

$$Q(r, z) = Nn(r, z)\overline{\sigma_i v}(z) \tag{5}$$

where N is the neutral density, assumed uniform, and $\sigma_i(v)$ is the ionization cross section, which depends on z through $T_e(z)$. We have implicitly neglected any radial variation of T_e and taken $n(r)$ to be the profile measured at z =24 cm. Since each of the quantities in equation (4) can be calculated from the measured profiles, we can evaluate both sides of equation (4) and numerically integrate over the discharge volume using the experimental data. This gives

$$N \int_0^L \overline{\sigma_i v}(z) \left[\int_0^a n(r, z) 2\pi r \, \mathrm{d}r \right] \mathrm{d}z = 2\pi a \int_0^L D_a(a, z) \left[\frac{\partial n(r, z)}{\partial r} \right]_{r=a} \mathrm{d}z. \tag{6}$$

The axial losses have been neglected, since both the axial gradients and the density at the ends are small in our large-aspect-ratio tube.

4.4.1. ICP mode. Because of the insulating wall, the radial diffusion at each position z has to be ambipolar, with a diffusion coefficient given by

$$D_a = \frac{\mu_e D_i + \mu_i D_e}{\mu_e + \mu_i} \tag{7}$$

where

$$D_e(r, z) = D_{e\parallel} = KT_e(z)/m\nu_e(r, z) \tag{8}$$

and

$$\mu_{e,i} = eD_{e,i}/KT_{e,i}. \tag{9}$$

The ion mobility was obtained from Ellis *et al* [21]. The electron transport coefficients were evaluated taking ν_e to be the sum of the electron-ion collision frequency ν_{ei} and the electron-neutral collision frequency ν_{en}, where, for n in cm^{-3},

$$\nu_{ei}(r, z) = 2 \times 10^{-6} n(r, z) \ln \Lambda / [T_e(z)(eV)]^{3/2} \tag{10}$$

$$\nu_{en}(z) = N\overline{\sigma_m v}(z). \tag{11}$$

Though electron–ion collisions dominate on axis, electron–neutral collisions dominate at the edge, where diffusion losses are computed.

The ionization rate for the ICP discharge was calculated at each axial location by integrating the ionization cross section provided by Kushner [22] over the measured Maxwellian distribution functions. The integrands of both sides of equation (6), representing respectively the number of ion-electron pairs created and the number lost to the walls per unit length per second, are shown in figure 17. These are seen to agree, to within a factor of two, consistent with the accuracy of the numbers used. Integrating over z, we find that the total particle production in the discharge to be 3.14×10^{20} s^{-1}, while the total radial loss is 1.92×10^{20} s^{-1}, well within the expected error.

Both the ionization rate and the radial loss rate can in turn be used to estimate the power lost in the plasma. Upon striking the wall, each pair of electrons and ions loses its kinetic energy, plus the energy radiated by inelastic collisions before the ionization took place. If the electrons are Maxwellian, the average energy W_i consumed in creating each electron-ion pair is a calculable function of electron temperature [23]. The plasma is connected to the insulating walls of the glass tube through a sheath and a presheath. The total energy W_t effectively carried out by each electron-ion pair lost is thus equal to

$$W_t(z) = 2KT_e(z) + \tfrac{1}{2}KT_e(z) + \tfrac{1}{2}KT_e(z) \ln(M/2\pi m) + W_i(z). \tag{12}$$

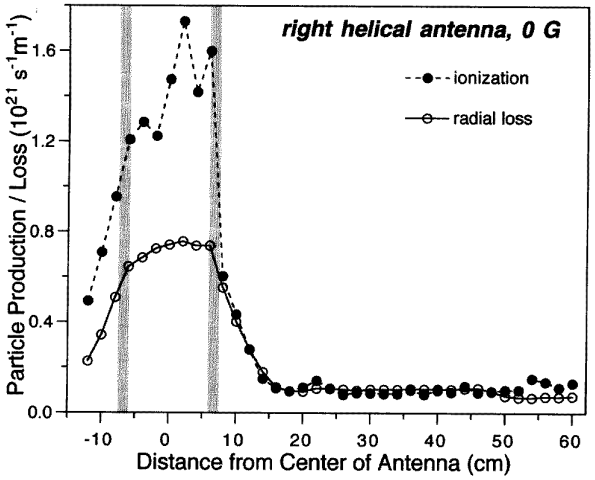

Figure 17. Axial variation of ion-electron production (●) and loss (○) rates calculated from the measured profiles for the 'standard' discharge at 0 G.

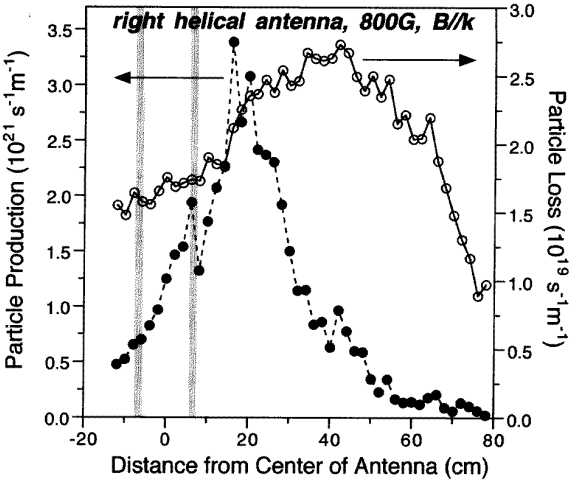

Figure 18. Axial variation of ion-electron production (●) and loss (○) rates calculated from the measured profiles for the 'standard' discharge at 800 G.

The first term corresponds to the average kinetic energy carried by an electron hitting the wall; the second term is the energy gained by each ion through the presheath; the third term is the energy gained by each ion through the sheath itself; and the last term is the energy lost in the creation of each electron–ion pair. The energy lost to heating the ions and to ion inelastic excitation is neglected. The total power can be obtained by multiplying the integrands of equation (6) by $W_t(z)$ and performing the integration. The calculated radial loss rate yields 2.0 kW of total power lost, while the calculated ionization rate yields 3.2 kW, compared with the measured RF power of 2.0 kW applied to the discharge. In view of the uncertainties in the data used, the agreement is good in both cases.

4.4.2. Helicon mode. In the 800 G helicon discharge, the ions can still be considered to be unmagnetized, but the thermal electrons have Larmor radii much smaller than the tube radius. Equation (8) must then be replaced by

$$D_e = D_{e\perp} = D_{e\parallel}/(1 + \omega_c^2/\nu_e^2) \tag{13}$$

where $\omega_c = eB/m$ is the electron cyclotron frequency. The value calculated for $D_{e\perp}$ is slightly smaller than that calculated for $D_{i\parallel}$, indicating that the radial ambipolar electric field should point inwards, contrary to the measured radial potential profile. The change of sign can easily result from small errors in these transport coefficients, since they are about equal. Therefore, for D_a we have used the average of $D_{e\perp}$ amd $D_{i\parallel}$. The resulting integrands of equation (6) are shown in figure 18. In this case the production and loss rates do not have the same z dependence. The discrepancy is not surprising in view of the anisotropy of the discharge. Electrons created at one location can travel rapidly along z to another and be lost there; indeed, the loss curve is broader than the production curve.

A more serious discrepancy is the disparity in magnitudes of the production and loss rates. If we integrate over z, the total production rate is calculated to be 9.4×10^{20} s^{-1}, while the integrated radial particle loss is 1.84×10^{19} s^{-1}. We have neglected ionization by Landau-accelerated electrons, since we did not expect this to be important at high densities; the ionization from thermal electrons alone appears to be almost two orders of magnitude too large. As in the case of the ICP discharge, the total power consumption can be estimated from these numbers. The former yields 11 kW, while the latter yields 214 W, both of which are in disagreement with the measured 2.0 kW of input power.

The underestimation of the particle loss and the overestimation of the production rate can be explained by considering the pumping effect due to the high degree of ionization in this kind of discharge. With no RF power, the neutral pressure is measured to be 15 mTorr, and the turbomolecular pump used provides 1.93×10^{19} particles s^{-1} of throughput, which is equal to the gas being fed into the chamber. This gas input q_0 remains constant when the discharge is on. The portion of neutral gas that is ionized is pumped out of the system at the ion acoustic velocity c_s, while the remaining gas flows out at its thermal speed:

$$q_0 \approx \bar{n} c_s A + P_n S(P_n)/KT_n \tag{14}$$

where $\bar{n}$ is the radially averaged electron density near the end of the tube, A is the cross sectional area of the tube, P_n is the gas pressure when the discharge is in operation, $S(P_n)$ is the pumping speed at this pressure, and T_n is the neutral gas temperature (300 K). Equation (14), with a density $\bar{n}$ of 2.5×10^{12} cm^{-3}, an electron temperature of 3 eV, and a pumping speed obtained from the manufacturer's data, yields a plasma-on pressure of approximately 4 mtorr, compared with the plasma-off pressure of 15 mtorr. With this new pressure the radial loss rate is increased to 7.36×10^{19} s^{-1}, yielding a new power consumption of 856 W, while the ionization rate is reduced to 2.36×10^{20} s^{-1}, yielding a new power loss of 2.8 kW. These are within a factor of two of the RF power of 2 kW, which is within

computational error. In this estimate of neutral depletion, we have neglected gradients of the neutral density. The mean free path of a room temperature neutral Ar atom against ionization by a 3 eV electron distribution of 2.5×10^{12} cm^{-3} density is about 150 cm, so that radial neutral gradients must be negligible, and axial gradients small. A more careful treatment of such gradients should eventually be done, but the data in this paper are not accurate enough to justify such a detailed analysis.

4.5. Electron temperature profile

The T_e profile in figure 10(a) has a peak at about 16 cm on the downstream side. That the profile is asymmetric with respect to the antenna shows that helicon wave propagation is involved in the heating. However, the electrons are apparently heated in a region within a wavelength of the antenna. The details of the physical mechanisms in this region are outside the scope of this paper. Downstream of the T_e peak, as we shall show, heating by the helicon wave is weak, and the T_e decay length is determined mainly by heat conduction and electron cooling by inelastic collisions. The heat flow equation in steady state is:

$$\frac{\mathrm{d}}{\mathrm{d}t}\left(\frac{3}{2}nkT_e\right) = -\nabla \cdot q + Q = 0 \tag{15}$$

where the source Q is given by

$$Q = Q_{wave} - Q_{inel} - Q_{elas} - Q_{\perp}. \tag{16}$$

Though the cross section data we used includes Q_{elas} due to neutrals, the losses Q_{elas} from elastic collisions with both ions and neutrals and $Q_{\perp}$ from cross-field diffusion are negligibly small. The heating term $Q_{wave} = \langle j_z E_z \rangle$ is also small in the downstream region, but we shall retain it. The term Q_{inel} due to excitation and ionization collisions with neutrals is the dominant one in Q; we have neglected the part due to ions. The heat flux q is given by [24]

$$\begin{aligned} q &= -\kappa_{\parallel}\frac{\partial}{\partial z}(KT_e) \\ \kappa_{\parallel} &= 3.2\frac{nKT_e}{m}\tau_e \\ \tau_e &= 3.44 \times 10^5 \frac{T_{eV}^{3/2}}{n \ln \Lambda}. \end{aligned} \tag{17}$$

Here T_{eV} is T_e in eV, and we have neglected the relatively infrequent collisions with neutrals. Note that the density n cancels out in q but would be expected to appear linearly in Q_{inel}.

The nature of the governing equation can be seen by neglecting the n dependence for the moment and taking $Q \approx Q_{inel}$ to be a function of T_e alone. Equations (15)–(17) then yield an equation of the form

$$\partial^2(T_e^{7/2})/\partial z^2 = f(T_e). \tag{18}$$

Defining

$$\begin{aligned} y &\equiv (T_e/T_0)^{7/2} \\ T_0 &\equiv T_e(z=0) \\ s &\equiv y_0' = y'(z=0) \end{aligned} \tag{19}$$

equation (18) takes the form

$$y'' = a^2 f(y) \tag{20}$$

where the constant a contains T_0 as well as the constants in equation (17). Multiplying equation (20) by y', we can integrate (20) to obtain

$$\tfrac{1}{2}(y'^2 - y_0'^2) = a^2 \int_1^y f(\eta)\,\mathrm{d}\eta \tag{21}$$

or

$$y'^2 = s^2 + 2a^2 \int_1^y f(\eta)\,\mathrm{d}\eta. \tag{22}$$

This can be integrated analytically for y for certain trial functions $f(y)$ such as $f(y) = y + c$ or $f(y) = 2\sin 2y$. Taking the simplest case $f(y) = y$, we obtain

$$\begin{aligned} y' &= \pm(s^2 - a^2 + a^2y^2)^{1/2} \\ z &= \pm \int_1^y \frac{\mathrm{d}\eta}{(s^2 - a^2 + a^2\eta^2)^{1/2}}. \end{aligned} \tag{23}$$

Taking the minus sign for a decaying temperature profile, we obtain a quadratic equation for y:

$$(a+s)\exp(-az) = ay + (s^2 - a^2 + a^2y^2)^{1/2}. \tag{24}$$

If $s^2 < a^2$, there is no solution for small y. If $s^2 > a^2$, the slope y' is finite at infinity ($y \to 0$). Thus, we must have $s^2 = a^2$, and the initial slope s is accurately specified by the asymptotic behaviour and the constant a.

For the actual data, we numerically integrated equation (15), keeping only the first two terms in equation (16). For Q_{wave}, we used the absolute amplitude $B_z(z)$ of the helicon wave measured previously [15] along the axis, averaging over the spatial oscillations arising from the beating of two modes. The ohmic heating term $\langle j_z E_z \rangle$ was computed from B_z using uniform-plasma theory, with $n(z)$ averaged radially. The corrections arising from radially nonuniform density are insignificant since Q_{wave} is small anyway. For Q_{inel}, we used the data compiled by Vahedi (see [23]), for the average energy loss for each ionization (a function of T_e) and multiplied by the ionization rate (a function of T_e), the locally measured values of n and the reduced neutral gas density. The resulting computed curve for $T_e(z)$, starting at the T_e peak, is shown in figure 19 in comparison with the data. Though $f(y)$ now depends on n as well as T_e, the initial slope of $T_e(z)$ is accurately determined by its asymptotic behaviour, as in the sample problem solved above. Here we have set the slope equal to zero at $z \approx 80$ cm, where the data end. The calculation agrees remarkable well with the data. Also shown in figure 19 is a curve computed without the term Q_{wave}. It is evident that downstream RF heating has little effect on the temperature profile. From the initial slope of $T_e(z)$, the heat flow downstream from the temperature peak can be calculated from equation (17). The result is $\approx$ 1.4 kW, showing that 70% of the RF input power is deposited in the antenna region and is then transported downstream. (We believe that the upstream flow is small). The following picture therefore emerges. Almost all the RF power is absorbed near the antenna, driving T_e to a

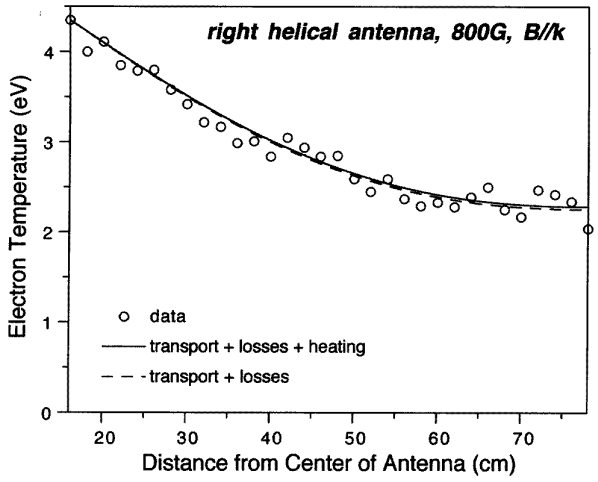

Figure 19. Decay of electron temperature downstream, as measured (○), and calculated with (——) and without (· · · · · ·) downstream wave heating.

peak at $z = 16$ cm, which is within a wavelength of the end of the antenna. Whether collisional or collisionless, the helicon absorption mechanism is extremely strong. Most of the absorbed energy is transported downstream by electron heat conduction and is lost by inelastic collisions with neutrals. The calculated energy loss agrees with both the temperature decay length and the total power that has to be dissipated. The temperature decay causes the density to rise downstream.

5. Conclusions

The axial dependence of plasma density, electron temperature, space potential, and ionized argon light emission have been measured for both right helical and Nagoya III antennas for various axial magnetic field values and directions. Our previous finding [14] that the $m = +1$ mode from radial wave profiles is preferentially excited is confirmed. The downstream behaviour unambiguously shows the beneficial effects of wave propagation and the difference between inductively coupled plasmas with $B = 0$ and helicon discharges with finite magnetic fields. In the latter case, the density is found to have a downstream peak which is not caused by increased ionization there. However, this effect can be explained in terms of pressure balance. The electron temperature profile shows that most of the plasma heating is done within a wavelength of the antenna, after which the temperature decays downstream with a scale length determined by heat conduction and inelastic collisions. Both the ionization rate and the particle loss rate computed from the measured profiles assuming no anomalous processes are in agreement with each other and with the RF input power. The importance of neutral depletion due to the ion pumping effect is pointed out, and the magnitude of this effect is given quantitively. For application to plasma processing, the deposition of RF energy near the antenna means that the device does not have to be very long; on the other hand, a longer device will permit the plasma to cool and become more dense, which are desirable characteristics for a remote source.

Acknowledgments

This work was supported by the Semiconductor Research Corporation, Contract No. 95-IJ-529, the National Science Foundation, Grant No. ECS 94-00849, by the Wisconsin Engineering Research Center for Plasma-Aided Manufacturing, and the Lawarence Livermore Laboratory Plasma Physics Research Institute.

References

[1] Boswell R W 1984 *Plasma Phys. Control. Fusion* **26** 1147
[2] Chen F F 1992 *J. Vac. Sci. Technol.* A **10** 1389
[3] Perry A J and Boswell R W 1989 *Appl. Phys. Lett.* **55** 148
[4] Charles C 1993 *J. Vac. Sci. Technol.* A **11** 157
[5] Kitagawa H, Tsunoda A, Shindo H and Horiike Y 1993 *Plasma Sources Sci. Technol.* **2** 11
[6] Jiwari N, Iwasawa H, Narai A, Sakaue H, Shindo H, Shoji T and Horiike Y 1993 *Japan J. Appl. Phys.* **32** 3019
[7] Benjamin N, Chapman B and Boswell R 1990 *Proc. SPIE* **95** 1392
[8] Campbell G A, de Chambrier A, Mendoza F, Parker N W, Pearson D I C, Tokunaga K, Tsukada T, Mashiro S and Nogami H 1992 *Proc. SPIE* **226** 1803
[9] Chen F F 1991 *Plasma Phys. Control. Fusion* **33** 339
[10] Komori A, Shoji T, Miyamoto K, Kawai J and Kawai Y 1991 *Phys. Fluids* B **3** 893
[11] Loewenhardt P K, Blackwell B D, Boswell R W, Conway G D and Hamberger S M 1991 *Phys. Rev. Lett.* **67** 2792
[12] Jiwari N, Fukasawa T and Kawakami H 1994 *J. Vac. Sci. Technol. A* **12** 1322
[13] Yasaka Y and Hara Y 1994 *Japan J. Appl. Phys.* **33** 5950
[14] Light M and Chen F F 1995 *Phys. Plasmas* **2** 1084
[15] Light M, Sudit I D, Chen F F and Arnush D 1995 *Phys. Plasmas* **2** 4094
[16] Chevalier G and Chen F F 1993 *J. Vac. Sci. Technol.* A **11** 1165
[17] Sudit I D and Chen F F 1994 *Plasma Sources Sci. Technol.* **3** 162
[18] Sanmartin J 1970 *Phys. Fluids* **13** 103
[19] Stangeby P C 1982 *J. Phys. D: Appl. Phys.* **15** 1007
[20] Imre A I, Daschchenko A I, Zapesochnyi I P and Kel'man V A 1972 *Sov. Phys.–JETP* **15** 503
[21] Ellis H W, Pai R Y and McDaniel E W 1976 *At. Data Nucl. Data Tables* **17** 177
[22] Kushner M 1994 Private communication
[23] Lieberman M A and Lichtenberg A J 1994 *Principles of Plasma Discharges and Materials Processing* (New York: Wiley) p 81
[24] Book D L 1987 *NRL Plasma Formulary* (Washington, DC: Naval Research Laboratory)